ORNL/TM-2017/274
Rev. 0

Synergies Between α' and Cavity Formation in HT-9 Following High Dose Neutron Irradiation

Nuclear Technology Research and Development

Prepared for
U.S. Department of Energy
Advanced Fuels Campaign
K.G. Field, B.P. Eftink, C.M. Parish,
T.A. Saleh, & S.A. Maloy
Oak Ridge National Laboratory
May 25th, 2017

SUMMARY

Candidate cladding materials for advanced nuclear power reactors, including fast reactor designs, require materials capable of withstanding high dose neutron irradiation at elevated temperatures. One candidate material, HT-9, through various research programs has demonstrated the ability to withstand significant swelling and other radiation-induced degradation mechanisms in the high dose regime (>50 displacements per atom, dpa) at elevated temperatures (>300°C). Here, high-efficiency, multi-dimensional scanning transmission electron microscopy (STEM) acquisition with the aid of a three-dimensional (3D) reconstruction and modeling technique is used to probe the microstructural features that contribute to the exceptional swelling resistance of HT-9. In particular, the synergies between α' and fine-scale and moderate-scale cavity formation is investigated.

CONTENTS

FIGURES

ACRONYMS

2D	Two-dimensional
3D	Three-dimensional
BF	Bright-field
dpa	displacements per atom
EDS	Electron-Dispersive X-ray Spectroscopy
EFTEM	Energy Filtered Transmission Electron Microscopy
FFTF	Fast Flux Test Facility
FIB	Focused Ion Beam
HAADF	High angle annular dark field
LAADF	Low angle annular dark field
LAMDA facility	Low Activation Materials Development & Analysis Facility
LANL	Los Alamos National Laboratory
MAADF	Medium angle annular dark field
MCR	Multivariate Curve Resolution
MVSA	Multivariate Statistical Analysis
ORNL	Oak Ridge National Laboratory
PCA	Principle Component Analysis
SDD	Silicon-Drift Detector
SEM	Scanning Electron Microscopy
STEM	Scanning Transmission Electron Microscopy
TEM	Transmission Electron Microscopy

SYNERGIES BETWEEN α' AND CAVITY FORMATION IN HT-9 FOLLOWING HIGH DOSE NEUTRON IRRADIATION

1. INTRODUCTION

HT-9 is a high chromium (>8 wt.% Cr) body centered cubic ferritic/martensitic steel used within the fossil fuel and nuclear industry for structural steel and fast reactor cladding applications [1]. The microstructure consists of a complex array of grains/grain boundaries including prior austenite grain boundaries, packet boundaries, and lath/lath boundaries. In the as-received state, the matrix is also populated with a variety of precipitates including inter- and intra-granular $M_{23}C_6$ carbides and intra-granular MX precipitates. A high number density of line dislocations will also be present in the microstructure.

The complicated microstructure of HT-9 lends itself to high dose neutron irradiations where swelling and other radiation-induced degradation mechanisms are a concern. Given this, the phase stability of HT-9 has been shown to be complex with the formation of α', G-phase, Chi, M_6C, and Laves to be possible under varying irradiation conditions [2]. The question remains on the role of radiation-induced and radiation-enhanced precipitation on the swelling resistance of HT-9. For instance, α' has been shown to precipitate in volume fractions as large as 4% with sub-10 nanometer sizes [2], but little attention has been paid towards the spatial and hence synergistic effects between α' and cavity formation. Internal interfaces within a microstructure have been shown to act as point defect sinks under irradiation [3,4] and hence one would anticipate if precipitation occurs prior to the on-set of steady state swelling that phase instabilities could contribute to the swelling resistance of HT-9.

Here, a high neutron dose irradiated HT-9 (155 displacement per atom (dpa), 443°C, Fast Flux Test Facility (FFTF), AC0-3 duct - Heat 84425 [2,5,6]) is used to investigate the synergistic effects between the formation of α', G-phase, and cavities. The composition of the HT-9 heat used can be found in Ref. [6]. To complete the study, high-efficiency multidimensional scanning transmission electron microscopy (STEM)-based acquisition combined with a 2-image tilt series three-dimensional (3D) reconstruction was used. The combined techniques allow for a rapid and robust means for visualization of the complex microstructure of HT-9 in 3D. The irradiation condition was selected as previous studies have indicated the presence of α', G-phase, and cavities within the irradiated microstructure [2,5,6].

2. METHODS

2.1 STEM-based experiments

STEM transparent lamellae were fabricated from bulk neutron irradiated HT-9 using a FEI Quanta 3D DualBeam Focused Ion Beam-Scanning Electron Microscope (FIB-SEM). Bulk neutron irradiated HT-9 was in the form of 1 mm discs from shear-punch tests obtained from Los Alamos National Laboratory (LANL). Primary fabrication and thinning was completed at 30 kV with final specimen thickness achieved using a 2 kV, 48-72 pA Ga^+ ion beam. A FEI Talos F200X S/TEM instrument operating at 200 kV was used for STEM and STEM-EDS acquisition within the Low Activation Materials Development and Analysis (LAMDA) facility at Oak Ridge National Laboratory (ORNL) [7]. A standard FEI double tilt analytical specimen holder was used. The FEI Talos F200X S/TEM is outfitted with a high brightness electron beam, four silicon-drift detector (SDD) X-ray detectors (total of 0.9 srad of collection angle), and four image detectors (bright field (BF), low-angle annular dark field (LAADF), medium angle annular dark field (MAADF) and high-angle annular dark field (HAADF)). The combination of these probes and detectors working in concert enabled the high-efficiency and high sensitivity multi-dimensional data

acquisition. Here, BF/MAADF/HAADF image triplets (1024×1024 pixels, 0.23 nm/pixel) and EDS spectrum data cubes (1024×1024, 0.23 nm/pixel, 60-minute acquisition time/map, 1.2 nA probe) were acquired at eucentric tilts of 0.51° and 20.55°. Image triplets were acquired prior to EDS acquisition while MAADF/HAADF pairs were collected simultaneously with the EDS acquisition. The BF detector was removed during the long EDS acquisition times to prevent chronic degradation of the detector. The EDS spectrum data cube-image pair acquisition was controlled using Bruker's Quantax Esprit software.

2.2 Multivariate statistical analysis

Sandia National Laboratories AXSIA code was used to complete multivariate statistical analysis (MVSA) [8]. Input into the AXSIA code was completed by converting raw data files from the Bruker Quantax Esprit software to acceptable AXSIA input files using a custom MATLAB script. MVSA was completed by binning the spectrum image data cube in 4×4 neighborhoods and the spectra by 2× in energy (keV) for energy analysis. The binned and truncated data was then scaled for Poisson noise [9,10] and analyzed using optimally-scaled principal component analysis (PCA). Following treatments included matrix rotations and de-scaling to convert the resulting data from Poisson space to real space. Multivariate curve resolution (MCR) under non-negativity constraints was used to convert the data into a format optimal for presentation purposes [11,12].

2.3 TEM-based experiments

Standard through-focus transmission electron microscopy (TEM) imaging was completed on a 200 kV JEOL JEM-2100F on the same region-of-interest. Images were taken at a defocus of 0 nm, ±500 nm and ±3000 nm at eucentric tilts of 0.2°, 10.6°, and 20.8°. Foil thickness was determined at zero tilt using Energy Filtered TEM (EFTEM) with a calculated mean free path length of 117.3 nm.

2.4 Tomographic reconstructions

A LANL developed proprietary software package built on the Python program language was used to develop reconstructions of the 3D volume. The software is optimized to reconstruct a 3D volume of precipitates, cavities, interfaces, and dislocations. Complex concave or convex curvatures/surfaces are not considered. Microstructural feature positions were determined using the combined images from the K-series lines of the Fe, Ni, and Cr as well as the HAADF image acquired in parallel.

3. RESULTS AND DISCUSSION

3.1 Microstructure and microchemistry analysis

Figure 1 shows the radiation-induced microstructure from a specific region of interest based on the multidimensional STEM (STEM imaging and STEM-EDS) acquisition. The microstructure proved to be complex with large (25-50 nm) G-phase precipitates rich in Ni, Si, and Mn, faint contrast from line dislocations (dark line contrast in Figure 1a), a large cavity central in the images and a population of sub-10 nm cavities (fine dark spots in Figure 1c). Figure 1 also highlights the importance of STEM-EDS based contrast as this acquisition mode is the only one capable of capturing the Cr-rich α' precipitates. The similar atomic numbers and minor lattice mismatch between α' precipitates and the α-Fe matrix means imaging α' using strain or Z-contrast techniques is inherently difficult. Figure 1 was generated from data taken at 0.51° eucentric tilt, the data from the 20.55° is not presented as the general microstructural features are identical between the two datasets.

Interestingly, Figure 1 provides indications that the α' precipitates are conjoined with the fine scale (<10 nm) cavities present in the matrix (i.e. the cavities have formed at the precipitate-matrix interface). This observation, at first pass, would indicate that the precipitation of α', which can occur on the order of hundreds or thousands of hours [13], influences the flux of point defects generated later within the

irradiation thereby effectively sequestering excess vacancies at the precipitate-matrix surface. This sequestration effect, and the high number density of α' within the matrix, could be a contributing factor to the excellent swelling resistance of HT-9.

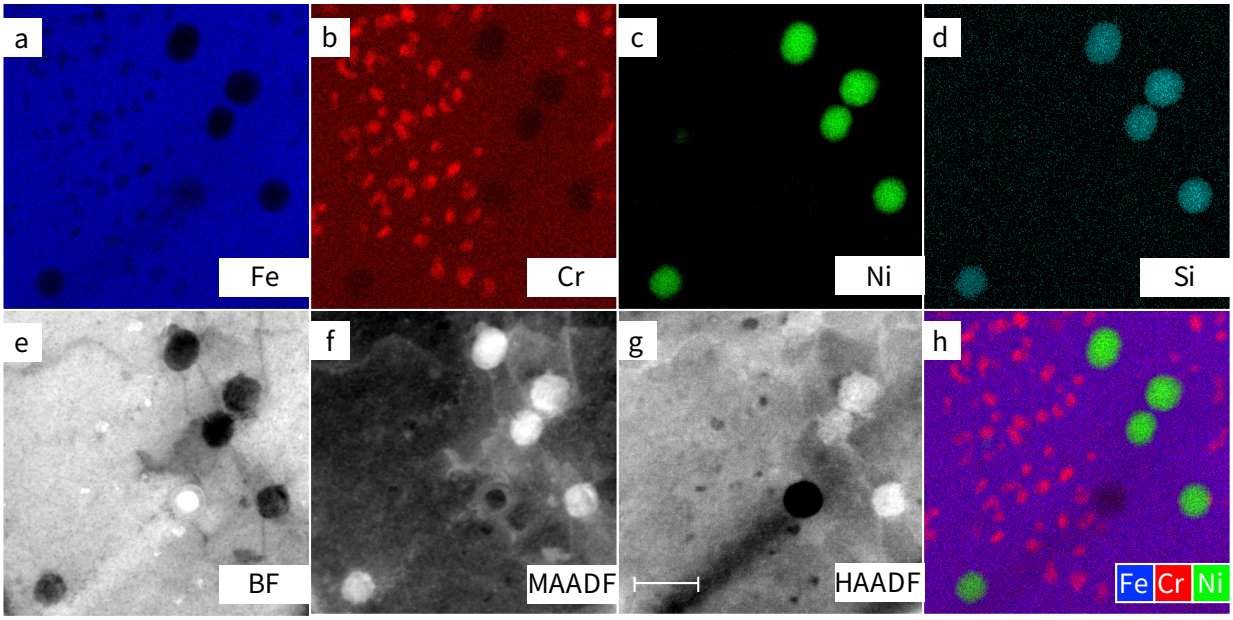

Figure 1: Two-dimensional (2D) dimensional projections of the 3D volume from the neutron irradiated HT-9 sample. Images formed via (a) K-series Fe, (b) K-series Cr, (c) K-series Ni, (d) K-series Si, (e) BF-STEM contrast, (f) MAADF contrast, (g) HAADF – Z-contrast, and (h) STEM-EDS color overlay contrast of K-series lines for Fe (blue), Cr (red), and Ni (green). Green-based contrast in overlay is G-phase and corresponds to dark contrast in BF, red-based contrast is α' precipitates – no diffraction or Z-contrast observed, and blue-based contrast is the Fe-rich matrix. Scale bar, 50 nm; all images of the same scale.

TEM through focus imaging was performed to confirm whether the fine-scale cavities in Figure 1 were indeed cavities and not low atomic number precipitates or other defects within the microstructure. Figure 2 shows the TEM images when tilted at 10° to eliminate additional strain/bend contour contrast within the micrographs. Figure 2 shows classical Fresnel-based contrast in the fine-scaled cavities enabling confirmation that the features of interest are the result of cavity-like elements within the matrix.

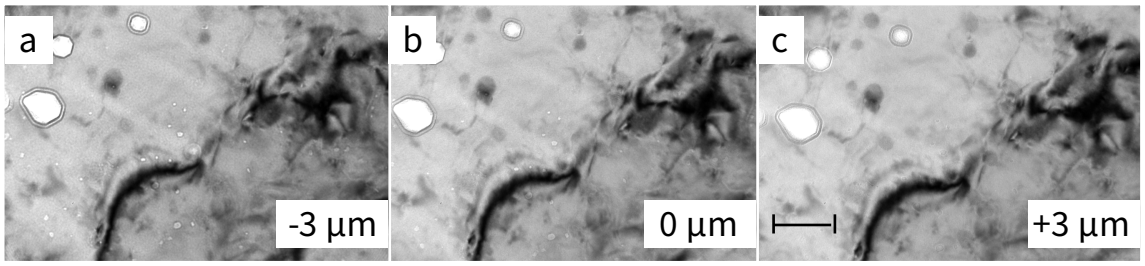

Figure 2: BF-TEM through focus images of the same region of interest shown in Figure 1. Note image is flipped and rotated between the two images and the current presentation shows a larger field of view. Scale bar, 100 nm; all images of the same scale.

Figure 1 also provides observational evidence that α' is denuded around the G-phase precipitates as previously reported in literature [2]. Given this, the proximity of several of the two different precipitate types provides some evidence that denudation is not uniform within the observed microstructure. An inherent issue with the presented observations and analysis is the data is presented as a 2D projection of a 3D volume. Features which could be largely separated through the thickness of the S/TEM lamellae could in-fact appear co-located or even conjoined within the specimen. To better analyze the microstructure and ultimately determine the synergies between the observed precipitation and cavity formation a novel 3D visualization technique based on a two-image tilt series was used.

3.2 3D reconstruction and model of microstructure

The 3D reconstruction was generated using several simplifying assumptions. First, only the observed cavities and precipitation were reconstructed, other features such as line dislocations and dislocation loops were not considered as careful tilting to keep these features in-constant in both tilt images was not conducted. Additional simplifications include approximating cavities as open volume spheres (i.e. faceting in the image was ignored) and both precipitate types were closed volume, perfect spheres. These simplifying assumptions enabled the use of a set of currently proprietary algorithms to be used on the two-image tilt series to conduct the 3D reconstruction.

Figure 3 shows the resulting projected volume images from varying perspectives of the 3D model (volume is 238 nm × 238 nm × 87-107 nm). The 3D model provides further insight into the spatial dependence of the different features of interest. For instance, Figure 3 shows that although the α' precipitates and both cavity populations are found within the same region of the neutron irradiated HT-9 specimen as indicated in the 2D projection in Figure 3, they are in fact not conjoined. 3D reconstructions were also conducted using the through-focus TEM imaging technique to verify that the observed location of the fine-scale cavities was correct. Both 3D models (TEM and STEM) shows the fine scale cavities to be located near the foil surface.

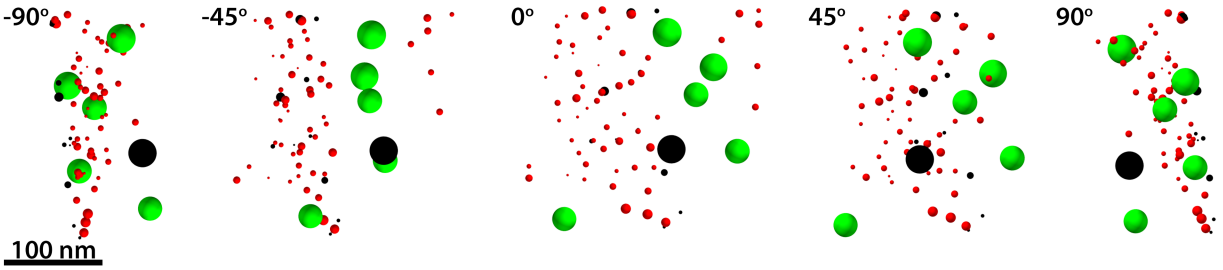

Figure 3: Projected volume images at varying orientations along the X-axis (top to bottom of the page) derived from the 3D model of the multidimensional data from the neutron irradiated HT-9 sample. Color scheme for precipitates is identical to the presentation in Figure 1, cavities are represented by black spheres.

Additional confirmation of the 3D model was completed using EFTEM and MVSA. Figure 3 indicates the microstructural features occupying a ~87 nm thickness in the foil thickness direction. The modeled specimen thickness can be confirmed using thickness maps from EFTEM as shown in Figure 4. Figure 4 shows that the same region of interest is estimated to have a thickness of ~107 nm, on average. EFTEM is known to have inaccuracies on the order ±20% or more in determining sample thickness[14]. Hence, it is not unexpected for the values of thickness between EFTEM and the 3D model to not match. As the model does not exceed the limiting values of the EFTEM map (with consideration of error), additional confidence is found in the 3D model of the observed region of interest.

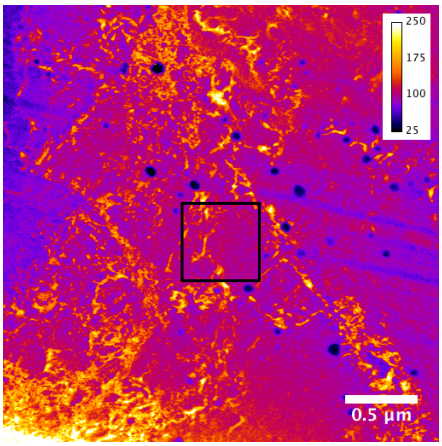

Figure 4: EFTEM thickness map for the region of interest (black bounding box) shown in Figure 1. Color calibration bar is in nm.

MVSA was used to provide insight into microstructural feature locations within the specimen volume by interpretation of the spectrum image based on correlated X-ray contributions. Specifically, MVSA determined the chemical rank within a sample and presents each independent X-ray (elemental) contributions as a loading spectrum and a score image. From this output, absorption differences within the embedded G-phase particles can be easily visualized. Absorption is expected to occur more strongly for lower energy X-rays positioned deepest within the specimen volume.

Figure 5 shows the resulting MVSA analysis and shows the signature of absorption differences within the 3rd and 4th (MVSA3 & MVSA4) loading spectra/score image pairs. MVSA3 within Figure 5c,e is of greatest interest as the independent elemental contributions indicate a strong Ni-L_α contribution to the loading spectra and score images. The Ni-L_α meets the requirements for strong absorption effects within the embedded specimen volumes. The precipitates labeled as #1 and #3 in Figure 5d show weak contrast in the score image suggesting strong absorption (if one assumes similar composition to other G-phase in the region of interest). Additionally, the G-phase precipitate labeled as #2 shows moderate contrast suggesting a mid-plane position within the specimen volume. Hence, the remaining, unlabeled, precipitates should reside near the specimen surface. This spatial relationship between the G-phase precipitates, as determined by the observed absorption effects in the MVSA analysis, confirms the computed spatial orientation within the 3D specimen volume from the 3D model presented in Figure 5. Based on the presented analysis, it is concluded that the 3D model is valid.

MVSA analysis also shows that Cr (MVSA2) is present throughout the matrix but higher concentrations can be observed in the α', indicative of the expected Cr-enrichment (>80 wt.% Cr) in this phase. It also indicates the α-Fe matrix still contains Cr in solid solution, as expected. Finally, MVSA3 and MVSA4 show the Ni-Si-Mn enrichment in the G-phase particles, as expected for G-phase, confirming the observed precipitates are indeed G-phase.

The two models (STEM and TEM-based) both indicated that the cavities were near or on the foil surface, hence confirming their real location within the specimen. The 3D model then leads to a different interpretation compared to the 2D microstructural representation in Figure 1. The observed spatial dependence between α' and the fine-scale cavities in the 3D model would suggest that although α' can demonstrate both misfitting semi-coherent and incoherent domains ($a_{\alpha'}$ = 2.88 Å, a_α = 2.87 Å) [15] they do not strongly sequester excess point defects that are produced under elevated temperature neutron irradiation at their interface between the precipitate and the matrix. Further systematic investigations are currently underway to determine the reasoning being the observed spatial relationships.

Figure 3 does confirm the presence of an α' denuded zone (~30 nm) around the larger-scale cavity and the G-phase particles indicating competition between the production of these defects under irradiation. The observed denudation is in agreement with the studies of Anderoglu et al. on the same heat of HT-9 [2]. The initial misinterpretation of the data from Figure 1 highlights the critical flaws/inaccuracies involved with 2D projection of a complex 3D microstructure such as the one presented here for HT-9.

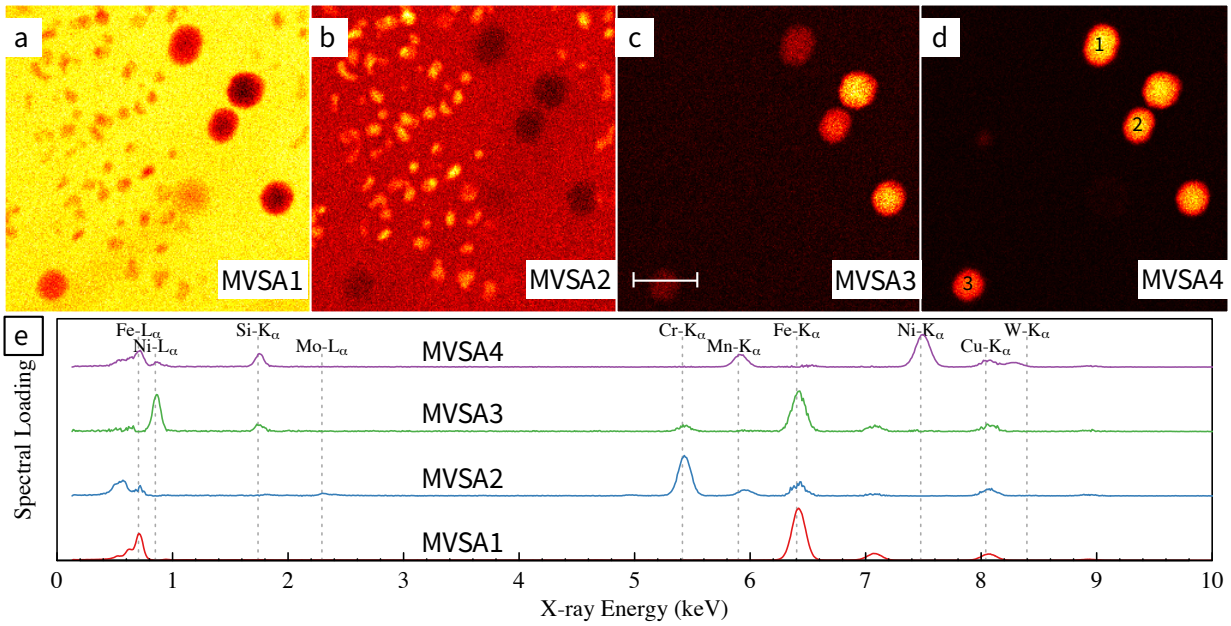

Figure 5: MVSA analysis of STEM-EDS generated spectrum image showing primary components of spectrum image. Spectrum image can be described with four components (a) MVSA1 – Fe-rich matrix, (b) MVSA2 – Cr-rich regions – α', (c & d) MVSA3/4– Ni-rich regions – G-phase. MVSA3 and MVSA4 arise due to absorption effects resulting in 'splitting' of the K-series and L-series Ni lines. Scale bar, 50 nm; all images of the same scale.

The use of high efficiency multi-dimensional STEM acquisition and rapid 3D modeling, as presented in this work, does highlight it's use within the nuclear materials field and other materials science fields of study. The technique offers a fast and robust means to visualize complex microstructures using multi-dimensional data across the length scales accessible using modern STEM instruments. The combination of modern characterization instrumentation with simplified 3D rendering stands as an alternative means towards advanced characterization compared to the extremely laborious STEM tomography based techniques currently being pursued in other fields of study.

4. CONCLUSIONS

A highly neutron irradiated (155 displacement per atom (dpa), 443°C) HT-9 specimen was investigated to determine the role of precipitation on cavity formation and swelling. The initial results presented here indicated that α' is co-located with fine-scale cavities within the irradiated microstructure but are not effective sinks for sequestration of point defects under the studied neutron environment. Additional observations included that α' remains denuded around the Ni-Si-Mn rich G-phase precipitates. These observations were made possible by completing high efficiency 3D visualization of the microstructure via multi-dimensional STEM acquisition and reconstruction.

5. ACKNOWLEDGEMENTS

The work presented in this report was supported by the Advanced Fuels Campaign of the Nuclear Technology R&D program in the Office of Nuclear Energy, US Department of Energy. This research was performed using instrumentation (FEI Talos F200X S/TEM) provided by the Department of Energy, Office of Nuclear Energy, Fuel Cycle R&D Program and the Nuclear Science User Facilities. The authors would like to thank T.J. Romero and M. Quintana for supplying the neutron irradiated HT-9 for this study. The authors are indebted to M.B. Toloczko, B. Makenas and W. Witherspoon of Pacific Northwest National Laboratory for the information describing the irradiation conditions of the AC0-3 duct and who led the retrieval of this duct for analysis.

6. REFERENCES

[1] R.L. Klueh, D.R. Harries, High-chromium ferritic and martensitic steels for nuclear applications, ASTM, 2001.

[2] O. Anderoglu, J. Van den Bosch, P. Hosemann, E. Stergar, B.H. Sencer, D. Bhattacharyya, et al., Phase stability of an HT-9 duct irradiated in FFTF, J. Nucl. Mater. 430 (2012) 194–204. doi:10.1016/j.jnucmat.2012.06.038.

[3] K.G. Field, L.M. Barnard, C.M. Parish, J.T. Busby, D. Morgan, T.R. Allen, Dependence on grain boundary structure of radiation induced segregation in a 9 wt % Cr model ferritic/martensitic steel, J. Nucl. Mater. 435 (2013) 172–180. doi:10.1016/j.jnucmat.2012.12.026.

[4] Y. Yang, K.G. Field, T.R. Allen, J.T. Busby, Roles of vacancy/interstitial diffusion and segregation in the microchemistry at grain boundaries of irradiated Fe–Cr–Ni alloys, J. Nucl. Mater. 473 (2016) 35–53. doi:10.1016/j.jnucmat.2016.02.007.

[5] B.H. Sencer, J.R. Kennedy, J.I. Cole, S.A. Maloy, F.A. Garner, Microstructural analysis of an HT9 fuel assembly duct irradiated in FFTF to 155dpa at 443°C, J. Nucl. Mater. 393 (2009) 235–241. doi:10.1016/j.jnucmat.2009.06.010.

[6] B.H. Sencer, J.R. Kennedy, J.I. Cole, S.A. Maloy, F.A. Garner, Microstructural stability of an HT-9 fuel assembly duct irradiated in FFTF, J. Nucl. Mater. 414 (2011) 237–242. doi:10.1016/j.jnucmat.2011.03.050.

[7] C.M. Parish, N.K. Kumar, L.L. Snead, P.D. Edmondson, K.G. Field, C. Silva, et al., LAMDA: Irradiated-Materials Microscopy at Oak Ridge National Laboratory, Microsc. Microanal. 21 (2015) 1003–1004. doi:10.1017/S1431927615005814.

[8] P.G. Kotula, M.R. Keenan, J.R. Michael, Automated analysis of SEM X-ray spectral images: a powerful new microanalysis tool., Microsc. Microanal. 9 (2003) 1–17. doi:10.1017/S1431927603030058.

[9] M.R. Keenan, P.G. Kotula, Accounting for Poisson noise in the multivariate analysis of ToF-SIMS spectrum images, Surf. Interface Anal. 36 (2004) 203–212. doi:10.1002/sia.1657.

[10] M.R. Keenan, P.G. Kotula, Optimal scaling of TOF-SIMS spectrum-images prior to multivariate statistical analysis, Appl. Surf. Sci. 231 (2004) 240–244. doi:10.1016/j.apsusc.2004.03.025.

[11] M.H. Van Benthem, M.R. Keenan, Fast algorithm for the solution of large-scale non-negativity-constrained least squares problems, J. Chemom. 18 (2004) 441–450. doi:10.1002/cem.889.

[12] M.H. Van Benthem, M.R. Keenan, D.M. Haaland, Application of equality constraints on variables during alternating least squares procedures, J. Chemom. 16 (2002) 613–622. doi:10.1002/cem.761.

[13] S.A. Briggs, P.D. Edmondson, Y. Yamamoto, C. Littrell, R.H. Howard, C.R. Daily, et al., A

combined APT and SANS investigation of alpha prime phase precipitation in neutron-irradiated model FeCrAl alloys, Acta Mater. 129 (2016) 217–228.

[14] T. Malis, S.C. Cheng, R.F. Egerton, EELS log-ratio technique for specimen-thickness measurement in the TEM, J. Electron Microsc. Tech. 8 (1988) 193–200. doi:10.1002/jemt.1060080206.

[15] J. Ribis, S. Lozano-Perez, Orientation relationships and interface structure of α-Cr nanoclusters embedded in α-Fe matrix after α-α' demixing in neutron irradiated Oxide Dispersion Strengthened material, Mater. Lett. 74 (2012) 143–146. doi:10.1016/j.matlet.2012.01.115.